Three-dimensional hollow urchin α-MnO_2 for enhanced catalytic activity towards toluene decomposition in post-plasma catalysis

Shiling Yang[a,b], Huachao Yang[a,b], Jinyuan Yang[a,b], Hualei Qi[a,b], Jing Kong[a,b], Zheng Bo[a,b,*], Xiaodong Li[a], Jianhua Yan[a], Kefa Cen[a], Xin Tu[c]

[a] *State Key Laboratory of Clean Energy Utilization, Institute for Thermal Power Engineering, College of Energy Engineering, Zhejiang University, Hangzhou, Zhejiang Province, 310027, China*

[b] *Hangzhou Global Scientific and Technological Innovation Center, Zhejiang University, Hangzhou, Zhejiang Province, 310027, China*

[c] *Department of Electrical Engineering and Electronics, University of Liverpool, Liverpool L69 3GJ, UK*

* Corresponding authors. Tel: +86 571 87951369, Fax: +86 571 87951616, E-mail address: bozh@zju.edu.cn

Abstract

Complete oxidation of volatile organic compounds (VOCs) with high energy efficiency remains a challenge in post-plasma catalysis (PPC) due to insufficient adsorption towards gas and relatively low catalytic activity at room temperature. Three-dimensional (3D) hollow urchin α-MnO_2 for post-plasma catalytic decomposition of toluene is demonstrated in this study. Hollow urchin catalyst assembled by well-defined one-dimensional (1D) α-MnO_2 nanorods is prepared by a simple one-step hydrothermal method without any template. The toluene decomposition, CO_2 selectivity and carbon balance over hollow urchin α-MnO_2 reach up to ~100%, ~59% and ~81% at an SIE of 240 J L^{-1}, which are 43%, 96% and 44% superior to that of non-thermal plasma (NTP) process, respectively. The combination of NTP with hollow urchin α-MnO_2 also significantly promotes the energy efficiency by 64%, reaching 13.1 g kWh^{-1} at an SIE of 119 J L^{-1}. Moreover, hollow urchin α-MnO_2 exhibits higher catalytic activity for toluene decomposition and ozone conversion compared with solid urchin α-MnO_2. The hollow structure with an enlarged contact surface area is expected to enhance adsorption towards gas and prolong the retention of gas on the catalyst surface. Furthermore, the fully exposed non-agglomerated 1D α-MnO_2 nanorods can promote oxygen vacancy density and low-temperature reducibility, facilitating the adsorption and conversion of ozone into active oxygen species (~100% ozone conversion), which leads to the deep decomposition of toluene in PPC. This work explores a new concept in designing 3D hollow urchin nanoarchitecture as a novel catalyst for efficient plasma-catalytic gas purification.

Keywords: Post-plasma catalysis; Toluene decomposition; Ozone conversion; Hollow urchin; α-MnO_2.

1. Introduction

The decomposition of volatile organic compounds (VOCs) is a crucial topic in environmental purification [1]. Among the various VOC decomposition methods, plasma catalysis has been demonstrated to be highly efficient, due to its high removal efficiency and selectivity towards CO_2 [2, 3]. Heterogeneous catalysts can be coupled with the non-thermal plasma (NTP) in two different ways: post-plasma catalysis (PPC, catalysts placed downstream of the NTP region) and in-plasma catalysis (IPC, catalysts packed inside the NTP region) [4, 5]. The combination of NTP and catalysts can induce plasma-catalysis synergy, promoting the removal of VOCs and CO_2 selectivity [6]. Compared with IPC, PPC can effectively utilize the plasma generated ozone as a source of active oxygen, resulting in less ozone emission [7-9].

The effective conversion of ozone into active oxygen over catalyst surface is of great importance to achieve superior VOC decomposition efficiency and high CO_2 selectivity in PPC [10, 11]. Various transition metal oxide catalysts (e.g. Mn, Co, Ce) have been proved to be efficient for the conversion of VOC and ozone [12-14]. Among these metal oxides, MnO_2 has been regarded as one of the most effective catalysts [10, 15]. MnO_2 catalysts with different phase structures have been investigated for post-plasma catalytic decomposition of VOCs [16]. α-MnO_2 was demonstrated to be superior to β-MnO_2 and γ-MnO_2 for VOC decomposition and conversion into CO_2, which is resulted from the abundant OH groups, excellent adsorption capacity and high mobility of oxygen. On the other hand, MnO_2 has been supported on various porous supports (e.g. γ-Al_2O_3 [16, 17], activated carbon [18] and zeolites [19, 20]) for

enhancing the catalytic activity due to the relatively high adsorption ability and enhanced catalyst dispersion. However, complete conversion of ozone and VOCs with high energy efficiency over the MnO_2 catalysts is still challenging due to insufficient adsorption towards gas at high gas flow rates and relatively low catalytic activities at room temperature. As a result, it is desirable to fabricate the MnO_2 catalysts with large contact surface area and high catalytic activity.

Hollow structures have attracted considerable attention due to their well-defined interior voids, high specific surface areas and excellent permeation properties [21, 22]. The hollow interior with a macroporous structure has a high surface-to-volume ratio, leading to improved transport diffusion, which could facilitate the adsorption of VOC molecules [23, 24]. In addition, the hollow structure is supposed to capture more ozone for generating active oxygen species resulting from the prolonged retention of ozone on the catalyst surface, thus promoting the oxidation of VOCs [25]. On the other hand, one-dimensional (1D) α-MnO_2 nanorods exhibit good catalytic activity for the removal of toluene due to the abundant surface oxygen species and excellent low-temperature reducibility [26]. Therefore, directly assembling 1D α-MnO_2 nanorods into a three-dimensional (3D) freestanding hollow nanoarchitecture is expected to have great potential for simultaneously enhancing adsorption towards gas and catalytic activity at room temperature, leading to superior ozone conversion and VOC decomposition in PPC.

Herein, we reported 3D hollow urchin α-MnO_2 for post-plasma catalytic decomposition of toluene. Hollow urchin nanoarchitecture assembled by well-defined

1D α-MnO_2 nanorods was prepared via a simple one-step hydrothermal method without any template. By comparison, solid urchin α-MnO_2 without hollow interior was synthesized by tuning the duration of hydrothermal treatment. We aimed for a systematic study of the plasma-catalytic oxidation of toluene over the solid urchin and hollow urchin α-MnO_2. Firstly, the resulting hollow urchin α-MnO_2 was endowed with larger specific surface area, increased oxygen vacancy density, higher surface oxygen concentration and better low-temperature reducibility compared with solid urchin α-MnO_2. Secondly, toluene decomposition, energy efficiency, ozone conversion, CO_2 selectivity and carbon balance over solid urchin and hollow urchin α-MnO_2 were investigated in detail. Finally, the main reaction pathways of toluene in the post-plasma catalytic process were proposed based on the formation of reactive species and organic intermediates.

2. Experimental section

2.1. Catalyst synthesis

Solid urchin and hollow urchin α-MnO_2 were fabricated by a one-step hydrothermal method. 1.262 g $KMnO_4$ (Sinopharm Chemical Reagent) was dissolved in 85 mL deionized water. Then 2 mL sulfuric acid (98 wt.%) was added into the $KMnO_4$ solution under stirring. Thereafter, 0.678 g Cu foil was immersed in the solution, which was then transferred to an autoclave. The Cu foil was always in the $KMnO_4$ solution during the hydrothermal reaction. The autoclave was kept at 110 ^oC in an oven for 6 or 12 h to synthesize solid urchin or hollow urchin MnO_2, respectively. After cooling to room temperature naturally, the precipitate was filtered, washed with

deionized water several times and dried at 80 ^{o}C in an oven for 12 h. The sample was first tableted, then crushed and sieved to 60-80 mesh.

2.2. Characterization

The surface morphologies of solid urchin and hollow urchin α-MnO_2 were investigated by scanning electron microscope (SEM, SU-70, Hitachi). The microstructures were characterized by transmission electron microscopy (TEM, JEM-2100, JEOL). The crystalline structures of the catalysts were inspected by X-ray diffraction (XRD, X'Pert powder, PANAlytical B.V.). Raman spectra were measured on a LabRAM HR Evolution Raman spectrometer (Horiba Jobin Yvon). The chemical compositions of the MnO_2 catalysts were confirmed by X-ray photoelectron spectroscopy (XPS, XR3E2, VG Escalab Mark II). All binding energies of the elements were calibrated using the contaminant carbon (C 1s = 284.6 eV) as a reference. N_2 adsorption-desorption isotherms were recorded by Autosorb-1-C instrument (Quantachrome Instrument) at −196 ^{o}C. Specific surface area (SSA) was calculated using Brunauer−Emmett−Teller (BET) method. Pore-size distribution was determined by the Barrett−Joyner−Halenda (BJH) method. The hydrogen temperature-programmed reduction (H_2-TPR) analysis of the MnO_2 catalysts was performed on a chemisorption analyser (Autochem II 2920, Micrometrics).

2.3. Experimental set-up

As shown in Fig. 1, the post-plasma catalytic system for toluene decomposition

consisted of a plasma generator, a coaxial dielectric barrier discharge (DBD) reactor, a packed-bed catalytic reactor, a gaseous toluene supply system and a gas-analysis system. The typical DBD reactor was composed of a quartz tube (external diameter of 8 mm and inner diameter of 6 mm), a ground electrode (10 mm-long aluminum foil wrapped around the quartz tube) and a high voltage electrode (a stainless-steel rod with a diameter of 4 mm placed on the axis of the quartz tube). The high voltage electrode was connected to the high-voltage alternating-current plasma generator (CTP-2000K, Suman Plasma Technology). The output frequency of the plasma generator was kept at 9.6 kHz during the experiment. The signals of voltage and current of discharge were recorded using a digital oscilloscope (MDO 3034, Tektronix). The catalyst (200 mg catalyst diluted with 2 g quartz sand) was packed into the catalytic reactor and placed downstream of the DBD reactor. Quartz sand is an inert material for the dispersion of catalyst. Mixing the catalyst with quartz sand led to sufficient contact between gas and the catalyst surface [27]. The length and diameter of the catalyst bed were 2 and 1 cm, respectively. Meanwhile, the distance between the DBD reactor and the catalyst bed was 8 cm. During the experiment, the total gas flow rate of the carrier gas (air, Gingergas) was fixed at 500 mL min^{-1} by a mass flow controller (MFC, D08−3F, Sevenstars), corresponding to a gas hourly space velocity (GHSV) of 19108 h^{-1}. A high-resolution syringe pump (LSP01-1BH, Longer Precision Pump) combined with a toluene generator (FD-PG, Friend Laboratory Equipment) was used to generate 145 ppm gaseous toluene in air. Liquid toluene with a flow rate of 10 μL h^{-1} was injected into the toluene generator. A gas chromatography (GC9790Plus, Fuli Instruments)

equipped with two flame ionization detectors and a reformer furnace was used to determine the concentrations of toluene, CO_2 and CO. The concentration of ozone was confirmed by an on-line ozone monitor (Models 106-MH, 2B Technology). The optical emission spectrum (OES) of reactive species in the discharge region was recorded in the range of 300-500 nm using a spectrometer (USB4000, Ocean Optics). The organic byproducts generated in the plasma-catalytic reaction were analyzed by gas chromatography with mass spectrometry (GC-MS, QP2010SE, Shimadzu). The outlet gas was collected by hexane solution with an adsorption time of 20 min for the GC-MS test. The FT-IR spectra of byproducts and adsorption breakthrough curves of toluene were recorded using an online multi-component analyzer (Gasmet Dx4000, Finland). For the dynamic adsorption process, 200 mg catalyst (60-80 mesh) was packed into a quartz tube with quartz wool plugged at the top and button. The initial concentration of toluene was kept at 105 ppm with a gas flow rate of 150 mL min^{-1}. The post-plasma catalytic decomposition of toluene was carried out at room temperature. The plasma was generated when the concentration of toluene at the outlet reached a steady state.

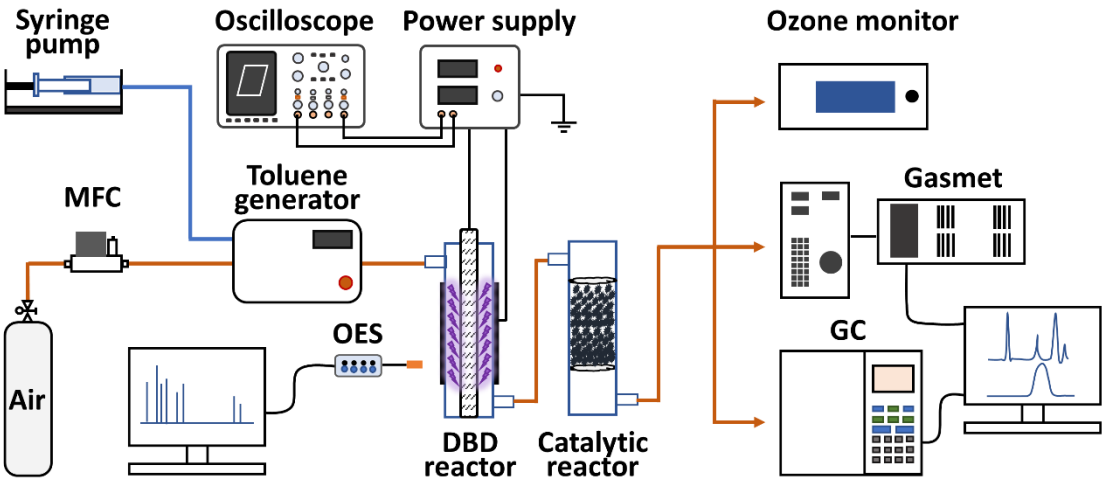

Fig. 1. Experiment set-up of the post-plasma catalytic decomposition of toluene.

The specific input energy (SIE), toluene decomposition ($\eta_{C_7H_8}$), energy efficiency (η_{EY}), ozone conversion (η_{O_3}), CO_2 selectivity (S_{CO_2}), CO selectivity (S_{CO}) and carbon balance of NTP and PPC processes are defined as:

$$\text{SIE (J L}^{-1}) = \frac{P}{Q} \times 60 \tag{1}$$

$$\eta_{C_7H_8}\,(\%) = \frac{[C_7H_8]_{in} - [C_7H_8]_{out}}{[C_7H_8]_{in}} \times 100 \tag{2}$$

$$\eta_{EY}\,(\text{g kWh}^{-1}) = \frac{3.6 \times M \times \left([C_7H_8]_{in} - [C_7H_8]_{out}\right)}{24.4 \times SIE} \tag{3}$$

$$\eta_{O_3}\,(\%) = \frac{[O_3]_0 - [O_3]_{out}}{[O_3]_0} \times 100 \tag{4}$$

$$S_{CO_2}\,(\%) = \frac{[CO_2]_{out}}{7 \times \left([C_7H_8]_{in} - [C_7H_8]_{out}\right)} \times 100 \tag{5}$$

$$S_{CO}\,(\%) = \frac{[CO]_{out}}{7 \times \left([C_7H_8]_{in} - [C_7H_8]_{out}\right)} \times 100 \tag{5}$$

$$\text{Carbon balance (\%)} = S_{CO_2} + S_{CO} \tag{6}$$

Where the input discharge power (P) of the DBD reactor is calculated using the Lissajous method; Q is the total gas flow rate; $[C_7H_8]_{in}$ and $[C_7H_8]_{out}$ are the inlet and outlet concentrations of toluene, respectively; M is the molar mass of toluene; $[O_3]_0$ and $[O_3]_{out}$ are the concentrations of ozone measured before and at the outlet of the catalytic reactor, respectively; $[CO_2]_{out}$ and $[CO]_{out}$ are the outlet concentrations of CO_2 and CO, respectively.

3. Results and discussion

3.1 Catalyst characterization

Hierarchical hollow urchin structure of MnO_2 is displayed in Fig.2. The hollow interior is expected to enhance adsorption towards gas and prolong the retention of gas on the catalyst surface. Moreover, the fully exposed non-agglomerated 1D MnO_2 nanorods can provide abundant active sites for the adsorption and conversion of ozone into active oxygen species (O*), which is favorable for the decomposition of toluene in PPC. Hollow urchin MnO_2 is synthesized by the facile one-step hydrothermal method without any template. Cu was used as a reducing reagent to reduce MnO_4^- into MnO_2. The redox reaction between $KMnO_4$ and Cu in acidic condition follows eq. (7) [28, 29]. The formation of hollow urchin MnO_2 follows the Ostwald ripening process (Fig. S1). The solid urchin grown from microsphere can transform into hollow urchin, accompanying with the depletion of core and the growth of nanorods.

$$2KMnO_4 + 3Cu + 4H_2SO_4 = 2MnO_2 + 3CuSO_4 + K_2SO_4 + 4H_2O \quad (7)$$

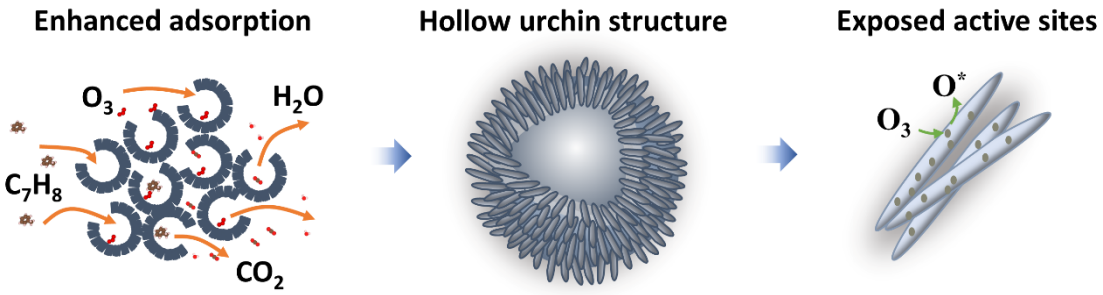

Fig. 2. Schematic illustration of hierarchical hollow urchin MnO_2 catalyst for toluene oxidation in post-plasma catalysis.

The morphologies and nanostructures of solid urchin and hollow urchin MnO_2 are

depicted in Fig. 3. Nanorods are uniformly grown on the intact surface of microspheres, forming the solid urchin structure with diameters of ~2 μm (Fig. 3a-b). The diameters of the assembled nanorods are ~20 nm. The HRTEM image further demonstrates that the single nanorod is well crystalline. The lattice spacing of 0.477 nm corresponds to the (200) lattice plane of α-MnO_2 (Fig. 3c) [30, 31]. As shown in Fig. 3d-e, compared with solid urchin MnO_2, the surface of hollow urchin MnO_2 was broken. The consumption of inner cores and the retained shells lead to the formation of open hollow urchin structure. The interior hollow cavity can enlarge the contact surface area exposed to gas and extend gas retention time. Moreover, 1D straight and radial nanorods with diameter of ~15 nm and length of ~1 μm exhibit sharp tip and non-agglomerated morphology, which could offer abundant active sites and facilitate the diffusion and adsorption of gas. The lattice spacing of 0.304 nm is indexed to the α-MnO_2 (310) plane (Fig. 3f) [32, 33]. The structural difference between solid urchin and hollow urchin MnO_2 was further investigated by TEM (Fig. S2). Solid urchin MnO_2 was composed of interior solid sphere and surface-distributed nanorods. On the contrast, a well-defined hollow cavity was observed in hollow urchin MnO_2, which was consistent with SEM results.

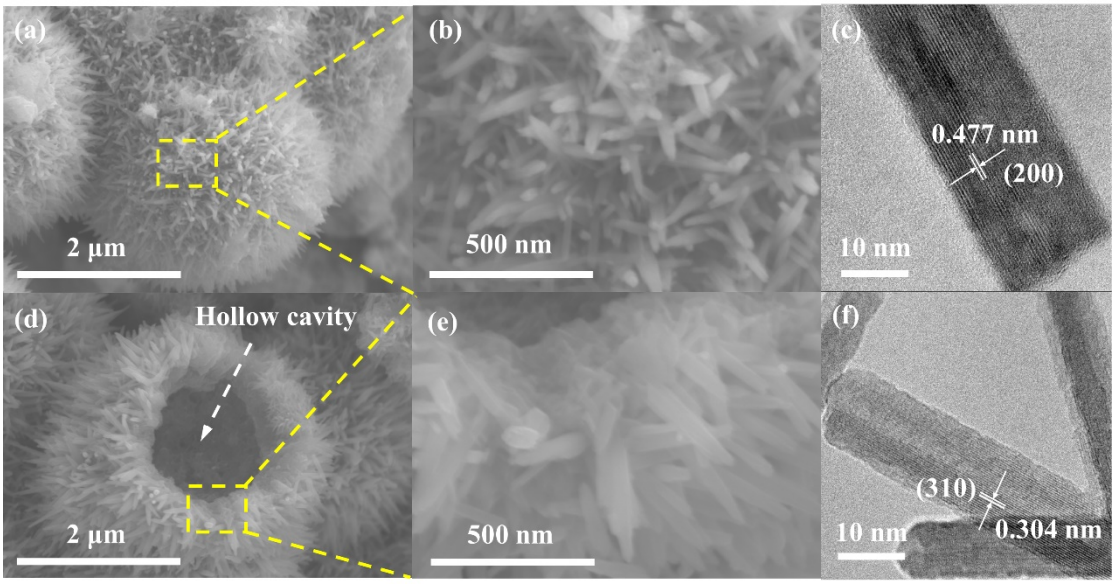

Fig. 3. SEM and HRTEM images of: (a-c) solid urchin and (d-f) hollow urchin MnO_2.

The crystal structures of solid urchin and hollow urchin MnO_2 are characterized by XRD. The XRD patterns are provided in Fig. 4a. All the characteristic peaks at around 12.5°, 17.7°, 28.5°, 37.3°, 41.8°, 49.6°, 56.1°, 60.0°, 65.2°, 69.2° and 72.8° match well with the (110), (200), (310), (211), (301), (411), (600), (521), (002), (541) and (312) diffraction of standard α-MnO_2 (JCPDS 44-0141) [34, 35], indicating the high purity and crystallinity of MnO_2, which is consistent with HRTEM results. Hollow urchin MnO_2 exhibits higher peak intensity and smaller peak width compared with solid urchin MnO_2, demonstrating the higher crystallinity and larger crystal size [36]. α-MnO_2 with double chains of edge-sharing MnO_6 octahedra forms 2 × 2 tunnels in the tetragonal unit cell, which is favorable for ozone adsorption and VOC decomposition [10, 37]. The crystallographic structures of α-MnO_2 catalysts are further investigated by Raman spectroscopy. As shown in Fig. 4b, two characteristic bands at 340 and 633 cm^{-1} are observed. The band at 633 cm^{-1} is indexed to the stretching modes of MnO_6

octahedra [38]. The band at 340 cm^{-1} represents the existence of α-MnO_2 [35]. It is found that hollow urchin MnO_2 exhibits slightly narrower peak, demonstrating the larger crystal size [39], which agrees with the XRD results.

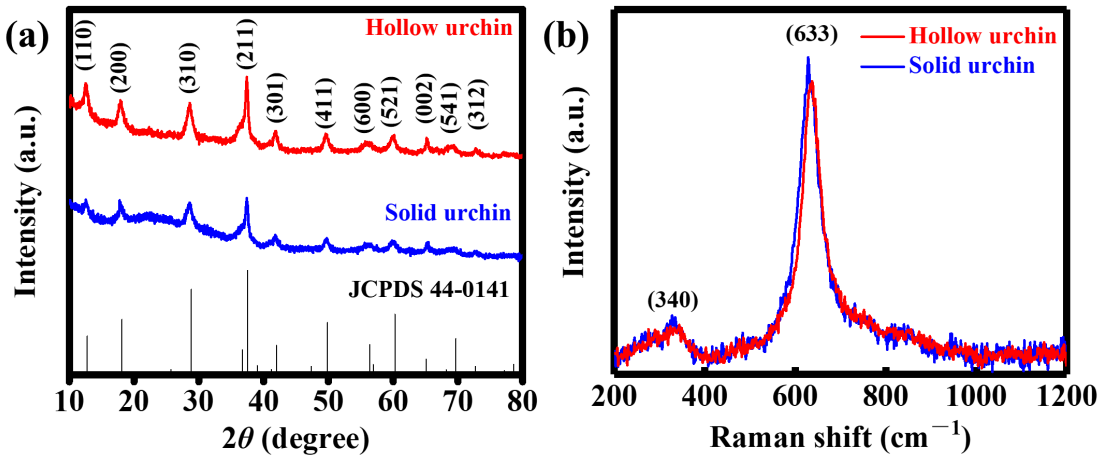

Fig. 4. (a) XRD patterns and (b) Raman spectra of solid urchin and hollow urchin α-MnO_2.

XPS spectra are employed to identify the valence states of transition-metal ions and oxygen species on the surface of catalysts. As shown in Fig. 5a, the full-range spectra of solid urchin and hollow urchin α-MnO_2 indicate the existence of Mn, O and C. The Mn 3s XPS spectra are sensitive to the valence states of manganese ions [40]. Therefore, the binding energy difference (ΔE) between the two peaks of the Mn 3s in XPS is used to calculate the average oxidation state (AOS) of Mn in manganese oxides [41, 42]. The calculation follows the equation: AOS = 8.956 – 1.126 × ΔE and the results are shown in Fig. 5b. The solid urchin and hollow urchin α-MnO_2 show separation energies of 4.72 and 4.80 eV, corresponding to the AOS of 3.62 and 3.53, respectively, which indicates an intermediate oxidation state between Mn^{4+} and Mn^{3+}.

The lower Mn AOS of hollow urchin α-MnO_2 is favorable for ozone conversion in comparison to solid urchin α-MnO_2, implying high a rate of toluene decomposition in PPC [43, 44].

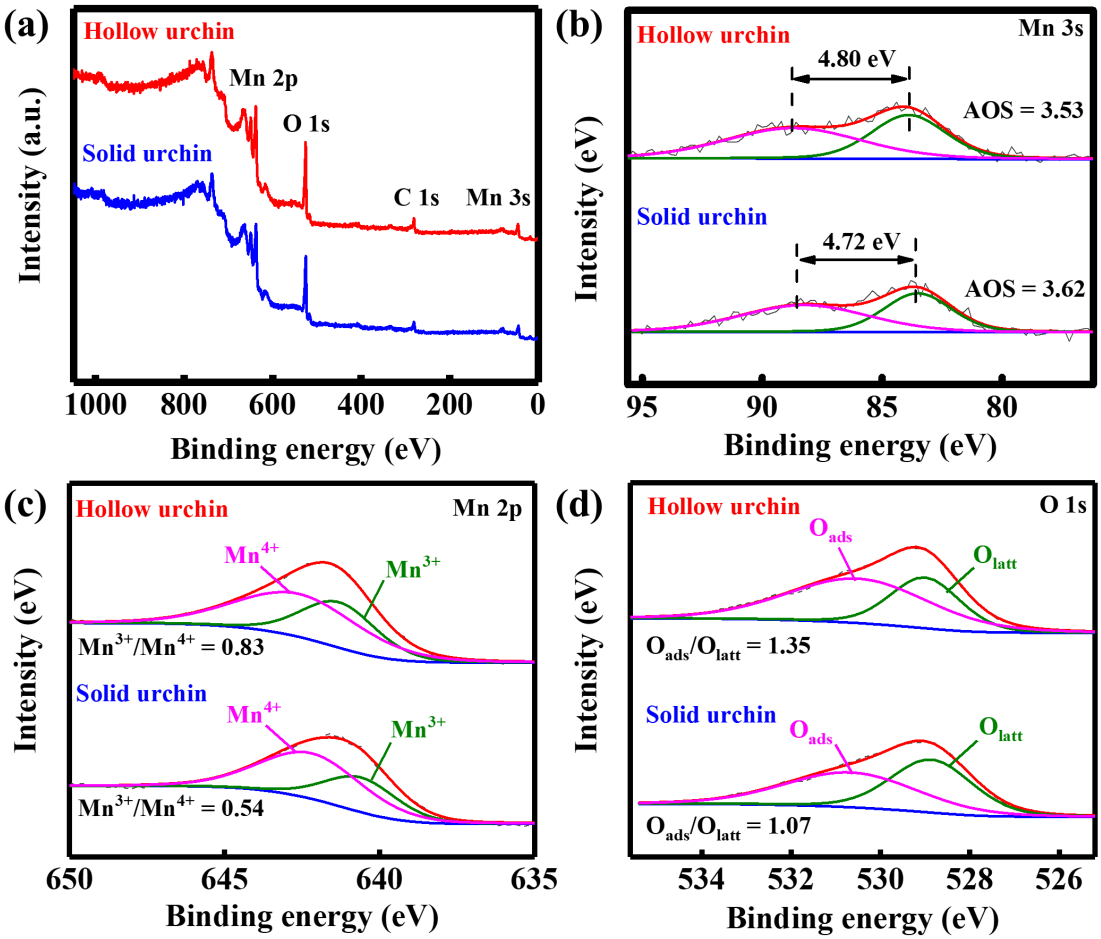

Fig. 5. (a) XPS survey spectra. Gaussian line fitted (b) Mn 3s, (c) Mn 2p and (c) O 1s spectra of solid urchin and hollow urchin α-MnO_2.

As displayed in Fig. 5c, Mn^{3+} (640.3-640.7 eV) and Mn^{4+} (642.3-642.8 eV) peaks can be deconvoluted from the Mn 2p spectra, representing that the Mn^{3+} and Mn^{4+} are the dominant valence states [13, 45, 46]. There exists no detectable Mn^{2+} species. The intermediate valence state Mn^{3+} ions have transforming ability between different

valence states to drive the redox cycles in the catalytic reaction [47]. Moreover, the presence of Mn^{3+} ions could lead to the formation of oxygen vacancies on the surface of MnO_2 due to electrostatic balance according to the following reaction (eq. 8) [48].

$$-Mn^{4+} - O^{2-} - Mn^{4+} - \rightarrow - Mn^{3+} - V_O - Mn^{3+} - + 1/2O_2 \quad (8)$$

Where V_O represents the oxygen vacancy. Therefore, the density of oxygen vacancies is in line with the existence of Mn^{3+} [10]. The content of Mn^{3+} can serve as an important parameter for evaluating the relative concentration of V_O. The oxygen vacancies could serve as the active sites for the adsorption and conversion of ozone to react with VOCs [44, 49]. The ratios of Mn^{3+}/Mn^{4+} of solid urchin and hollow urchin α-MnO_2 are calculated to be 0.54 and 0.83, respectively, demonstrating that more oxygen vacancies are formed on the surface of hollow urchin α-MnO_2, which is favorable for the oxidation of toluene. The transformation of solid urchin MnO_2 into hollow urchin MnO_2 could expose more MnO_6 edges, which facilitates the release of lattice oxygen to generate more surface oxygen vacancies [50, 51]. As depicted in Fig. 5d, the O 1s spectra are also fitted into two peaks, representing two different kinds of oxygen species, i.e. the lattice oxygen (O_{latt}) at 528.9-529.0 eV and the adsorbed oxygen (O_{ads}) 530.7 eV [52, 53]. The calculated ratios of O_{ads}/O_{latt} for solid urchin and hollow urchin α-MnO_2 are 1.07 and 1.35, respectively. The higher concentration of surface adsorbed oxygen means a larger amount of oxygen vacancies on the catalyst surface since the oxygen molecules are adsorbed on the oxygen vacancies [26]. According to previous literature, catalytic conversion of ozone over the catalyst surface relies on the involvement and recycling of oxygen vacancy and ozone could bind to MnO_2 by

inserting an O atom into surface oxygen vacancy [48]. Hence, higher density of oxygen vacancies on the surface of hollow urchin α-MnO_2 serve as active sites, which are expected to enhanced adsorption toward gas and induce more complete conversion of ozone and toluene in PPC.

The structures of solid urchin and hollow urchin α-MnO_2 are further investigated by the nitrogen adsorption-desorption measurements. All the MnO_2 catalysts exhibit similar typical type IV isotherms (Fig. 6a) [29]. The hysteresis loops in the low relative pressure (P/P_0) range of 0.45 to 0.95 might be attributed to mesoporous structures in the nanorods or cavities [54]. The BET SSA of solid urchin and hollow urchin α-MnO_2 is calculated to be 76.5 and 89.3 $m^2\ g^{-1}$, respectively. In addition, the BJH pore-size distributions further demonstrate the mesoporous structures of the α-MnO_2 catalysts (Fig. 6b) [28]. The average pore size of hollow urchin α-MnO_2 (15.9 nm) is bigger than that of solid urchin α-MnO_2 (15.1 nm), which may facilitate the adsorption toward gas [16]. The total pore volume of hollow urchin α-MnO_2 (0.306 $cm^3\ g^{-1}$) is slightly lower than that of solid urchin α-MnO_2 (0.315 $cm^3\ g^{-1}$), mainly ascribed to the increased crystallite size (from XRD results) [55]. Thus, with the depletion of cores and the growth of nanorods, the formed hollow cavity nanostructure and non-agglomerated shell enlarge the contact surface area. The high BET specific surface area and mesoporous structure of hollow urchin α-MnO_2 could provide abundant active sites for the catalytic reaction.

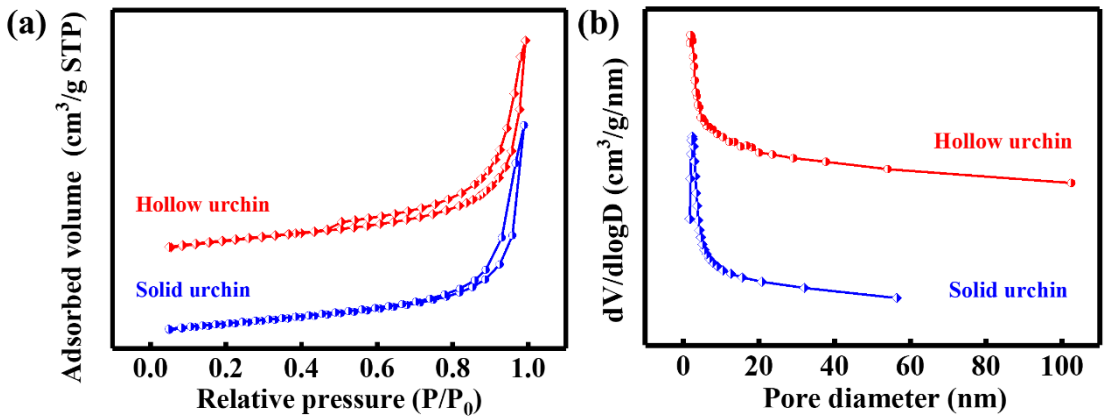

Fig. 6. (a) Nitrogen adsorption-desorption isotherms and (b) BJH pore-size distributions of solid urchin and hollow urchin α-MnO_2.

As shown in Fig. S3, the adsorption capacity of solid urchin and hollow urchin α-MnO_2 for toluene is further investigated. The breakthrough curves are the evolution of C/C_0 over time, where C and C_0 are the concentrations of toluene at the outlet and inlet, respectively [56]. The first breakthrough time ($t_{0.05}$, $C/C_0 = 0.05$) over hollow urchin α-MnO_2 (80 s) is prolonged compared with solid urchin α-MnO_2 (20 s). Hollow urchin α-MnO_2 also exhibits an increase in the amount of adsorbed toluene (1.86 mg g^{-1}) in comparison to solid urchin α-MnO_2 (1.42 mg g^{-1}). In addition, hollow urchin α-MnO_2 shows a more rapid increase in the curve after the breakthrough, indicating less diffusion resistance during the adsorption process [57]. Therefore, the formation of hollow urchin structure is favorable for gas adsorption and decomposition in the PPC process, which is in accordance with nitrogen adsorption-desorption measurement.

The redox properties of solid urchin and hollow urchin α-MnO_2 are evaluated by the H_2-TPR analysis. As displayed in Fig. 7, three peaks at 237, 264 and 287 ^oC are observed in the TPR profile of solid urchin α-MnO_2. The reduction peaks of H_2

consumption are attributed to the successive reduction processes: $MnO_2 \rightarrow Mn_2O_3 \rightarrow Mn_3O_4 \rightarrow MnO$ [58]. For the hollow urchin α-MnO_2, the starting reduction temperature is shift to 184 °C, significantly lower than that of solid urchin α-MnO_2. The reduction processes in the high temperature range are associated with the formation of Mn_3O_4 (239 °C) and MnO (282 °C) [26]. Compared with solid urchin α-MnO_2, the decreased reduction temperatures indicate the higher mobility of the oxygen species and improved low-temperature reducibility of hollow urchin α-MnO_2, which is favorable for ozone conversion and toluene decomposition [46, 52, 59].

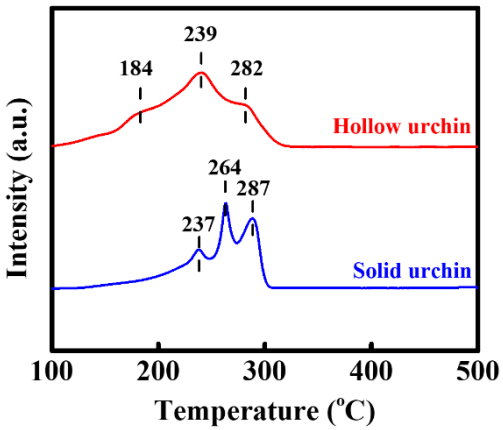

Fig. 7. H_2-TPR profiles of solid urchin and hollow urchin α-MnO_2.

3.2 Toluene decomposition

The oxidation of toluene as a function of SIE from 100 to 250 J L^{-1} in NTP and PPC processes are carried out and the corresponding reaction performance is displayed in Fig. 8. Toluene decomposition and energy efficiency are strongly influenced by the SIE. With the increment of SIE, toluene decomposition in NTP and PPC processes is significantly improved, mainly attributed to the enhanced generation of high-energy electrons and active species (Fig. 8a) [60]. While increasing the SIE leads to the

decrease of energy efficiencies in NTP and PPC processes (Fig. 8b). The promoting effect of MnO_2 catalysts on the oxidation of toluene is obvious. The toluene decomposition of hollow urchin α-MnO_2 reaches up to ~100% at an SIE of 240 J L^{-1}, which is 43% higher than that of NTP. The highest energy efficiency of NTP process is only 8.2 g kWh^{-1} at an SIE of 108 J L^{-1}. In contrast, the introducing of hollow urchin α-MnO_2 dramatically promotes energy efficiency, reaching up to 13.1 g kWh^{-1} at an SIE of 119 J L^{-1}. The increased energy efficiency could reduce the energy consumption of the plasma-catalytic decomposition of toluene. Note that hollow urchin α-MnO_2 exhibits higher rates of toluene decomposition and energy efficiency at low SIE range (119-222 J L^{-1}) in comparison to solid urchin α-MnO_2 (by 16% and 18%, respectively).

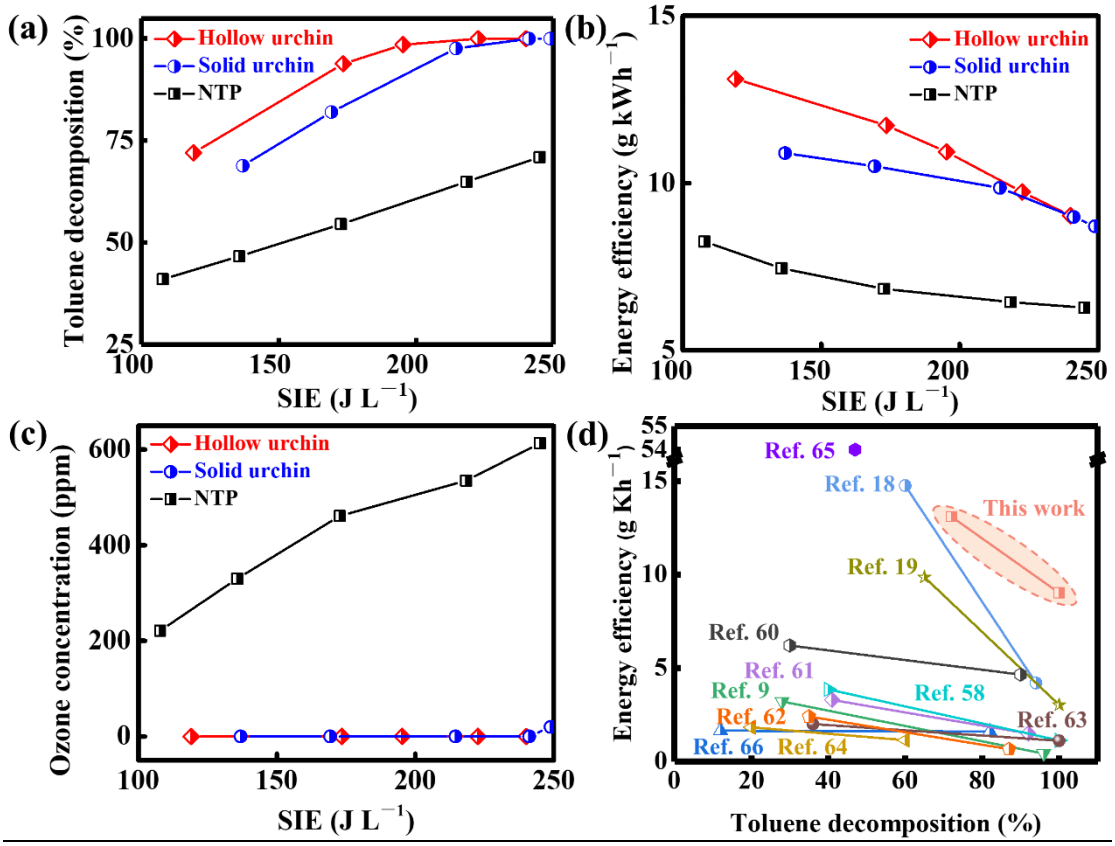

Fig. 8. (a) Toluene decomposition, (b) energy efficiency and (c) ozone concentration

in NTP and PPC processes. (d) Comparison of energy efficiency and toluene decomposition between our work and previous studies.

The enhanced oxidation of toluene by hollow urchin α-MnO_2 can be ascribed to the efficient ozone conversion over catalysts. As shown in Fig. 8c, nearly ~100% ozone conversion is achieved by introducing hollow urchin α-MnO_2. The concentrations of residual ozone over solid urchin and hollow urchin α-MnO_2 are 19.7 and 0 ppm at SIE of 249 and 240 J L^{-1}, respectively. The corresponding maximum ozone conversion capacities per gram catalyst are calculated to be 2968 and 3067 ppm g^{-1} for solid urchin and hollow urchin α-MnO_2, respectively, which are higher than that of previous studies [19]. The generated active oxygen species from ozone conversion could lead to deep oxidation of toluene and high energy efficiency [7, 61]. Compared with solid urchin α-MnO_2, the promoted conversion of ozone over hollow urchin α-MnO_2 can be attributed to the unique hollow structure for enhancing adsorption towards gas and the non-agglomerated morphology for promoting oxygen species concentration as well as low-temperature reducibility. Owing to the highly efficient ozone conversion, the toluene decomposition and energy efficiency over hollow urchin α-MnO_2 are 72-100% and 9.0-13.1 g kWh^{-1} in the SIE range of 100-250 J L^{-1}, respectively, which are among the best of state-of-the-art works in terms of toluene decomposition (Fig. 8d) [9, 19, 20, 60, 62-68].

The CO_2 selectivity and carbon balance of NTP and PPC processes are displayed in Fig. 9. The increase of SIE significantly promotes the selectivity towards CO_2 and

carbon balance. However, the formation of organic byproducts in the NTP process leads to the poor CO_2 selectivity and carbon balance [69]. Compared with the NTP process, the combination of NTP with hollow urchin α-MnO_2 remarkably enhances the conversion of toluene into CO_2 and carbon balance by 96% and 44%, reaching up to ~59% and ~81% at an SIE of 240 J L^{-1}, respectively, which can be ascribed to the improved oxidation of toluene and organic intermediates. In addition, the decreased CO selectivity and slightly increased CO concentration of PPC processes are also attributed to the further toluene decomposition over catalysts (Fig. S4) [17]. In the control experiment, the toluene decomposition over pure quartz sand is almost equal to that of NTP process, demonstrating the negligible catalytic effect of quartz sand on toluene decomposition (Fig. S5). Therefore, the enhanced performance in PPC process is mainly contributed by MnO_2.

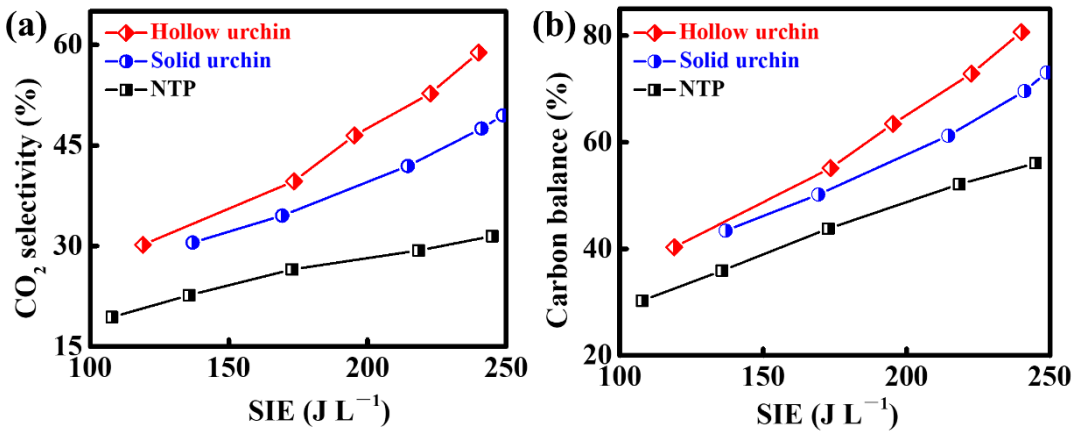

Fig. 9. (a) CO_2 selectivity and (b) carbon balance in NTP and PPC processes.

The catalytic durability of solid urchin and hollow urchin MnO_2 in PPC processes is further investigated. The SIE is kept at 248 J L^{-1}. As shown in Fig. S6, solid urchin MnO_2 exhibits obvious decay of catalytic performance (~23%). In contrast, toluene decomposition over hollow urchin MnO_2 is relatively stable during 8 h-test. With

increasing the reaction time, toluene decomposition decreases from 100% to 89%. XRD patterns of the spent catalysts indicate that both solid urchin and hollow urchin MnO_2 are still α-MnO_2 (JCPDS 44-0141) after the durability test (Fig. S7). Therefore, the observed deactivation is not resulted from the transformation of crystalline MnO_2. As shown in Fig. S8, Mn 3s spectra of the spent MnO_2 demonstrate that Mn AOS of solid urchin and hollow urchin MnO_2 increase from 3.62 and 3.53 to 3.75 and 3.61, respectively, which is mainly attributed to the oxidation of Mn^{3+} into Mn^{4+} by ozone in the PPC process, resulting in the validation of oxygen vacancies [48]. Importantly, the Mn AOS of spent hollow urchin MnO_2 is still lower than that of spent solid urchin MnO_2, implying better catalytic performance of hollow urchin MnO_2. Therefore, hollow urchin MnO_2 has potential as a promising catalyst for stable and efficient toluene decomposition.

3.3 Reaction mechanism

The formation of reactive species in the discharge region is analyzed by the OES. As shown in Fig. 10a, the OES ranging from 300 to 500 nm was recorded at an SIE of 245 J L^{-1} at atmospheric pressure. The characteristic emission spectra of the second positive bands of N_2 ($C^3\Pi_u \rightarrow B^3\Pi_g$) and the first negative bands of N_2^+ ($B^2\Sigma_u^+ \rightarrow X^2\Sigma_g^+$) resulting from the excitation, ionization, and dissociation reactions in plasma discharge are observed [70]. The formation of the strong bands of N_2 ($C^3\Pi_u \rightarrow B^3\Pi_g$) is ascribed to the large proportion of N_2 in gas [63]. In addition, the weak spectra of CN, CH, O_2^+ and H_γ are also detected [71]. The generated radicals and reactive species can collide

with gas molecules, leading to the destruction of toluene and organic intermediates.

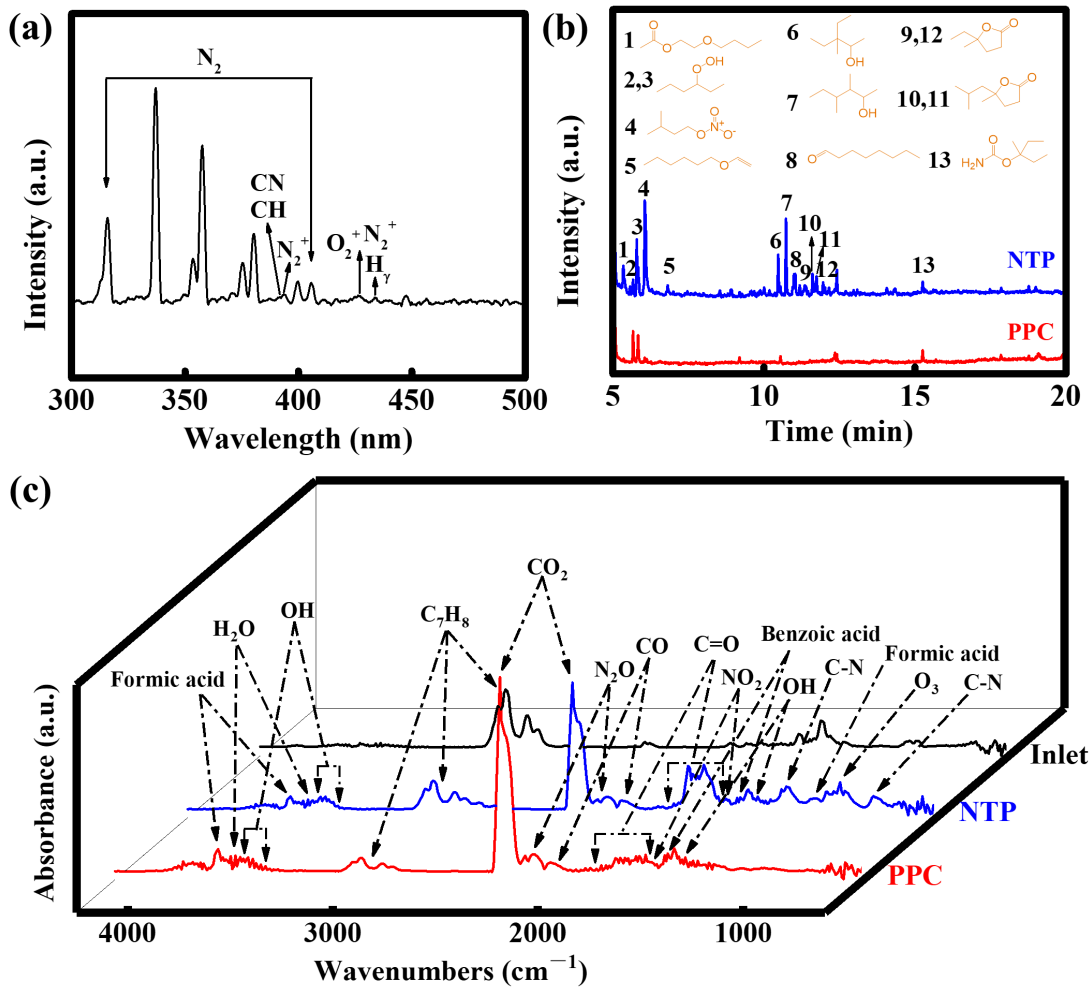

Fig. 10. (a) OES of plasma in the discharge region. (b) GC-MS diagrams and (c) FT-IR spectra of organic byproducts at the outlet gas of toluene decomposition in NTP and PPC processes.

The formation of organic byproducts in the post-plasma catalytic reaction is detected by GC-MS. As shown in Fig. 10b, ten types of ring-opening organic intermediates are identified in the NTP process, including hydrocarbons, acids, and so on (Table S1), which demonstrates the insufficient oxidation of toluene and poor selectivity towards CO_2. While the types and amounts of byproducts are significantly

reduced in the PPC process, indicating the deep conversion of toluene and organic byproducts due to the efficient ozone conversion over hollow urchin α-MnO_2.

Fig. 10c shows the FT-IR spectra of the gaseous products recorded at an SIE of 245 J L^{-1} in the NTP and PPC processes. Nitromethane, formic acid, benzoic acid, benzaldehyde, maleic anhydride and phenol are identified as the primary byproducts in the NTP process. In addition, H_2O, O_3, CO_2, CO, NO_2 and N_2O are also detected. The absorption bands at 895 and 1320 cm^{-1} are related to the C−N stretching vibration in the organic species with atomic N formed in the plasma (e.g. nitromethane) [16, 72]. The characteristic bands centered at 1181 and 3736 cm^{-1} are attributed to the formation of formic acid [73-75]. Bands located at 1559 cm^{-1} are assigned to benzoic acid [76, 77]. The C=O stretching vibrations in benzaldehyde and maleic anhydride are indicated by the absorption bands at 1636-1906 cm^{-1} [72, 78]. Features at 3500-3600 cm^{-1} are associated with OH groups (e.g. phenol and carboxylic acid) [79]. The organic byproducts are formed due to the collision between high-energy electrons/reactive species and toluene/air molecules [80]. Note that coupling NTP with catalyst remarkably reduces the amount of ozone, toluene and gas phase byproducts. The highly efficient conversion of ozone into active oxygen species in the PPC process leads to the improved oxidation of toluene and organic intermediates, further increasing the CO_2 concentration.

As displayed in Fig. 11, major degradation pathways of toluene in post-plasma catalytic process over hollow urchin α-MnO_2 catalyst are proposed based on the results of OES, GC-MS and FT-IR. The reaction mechanism consists of plasma-induced ring-

opening destruction of toluene in the gas phase (Fig. 11a) and the adsorption and conversion of toluene and organic byproducts into CO_2 and H_2O on the surface of the catalyst (Fig. 11b). Firstly, energetic electrons impact with N_2 and O_2 to generate radical species (e.g. $\cdot NO_2$, $\cdot OH$, $\cdot H$ and $\cdot O$), leading to the destruction of toluene molecule [62]. The hydrogen is abstracted from the methyl group due to the electron collision [77]. Subsequently, the formed benzyl radical could react with $\cdot OH$ or $\cdot O$ to generate benzaldehyde and further be oxidized into benzoic acid, as demonstrated in the FT-IR results [81]. Furthermore, the dissociation of C-C bond forms methyl and phenyl radicals. Methyl radicals can react with $\cdot NO_2$ and $\cdot OH/\cdot O$ to form nitromethane and formic acid, respectively [9]. The reactions between phenyl radicals and $\cdot OH$, $\cdot H$ as well as $\cdot NO_2$ could generate phenol, benzene and nitrobenzene, respectively [78]. After that, the aromatic intermediates can react with energetic electrons or active species ($\cdot H$, $\cdot OH$ and $\cdot O$), resulting in ring-open reactions and deep oxidation of byproducts into CO_2 and H_2O.

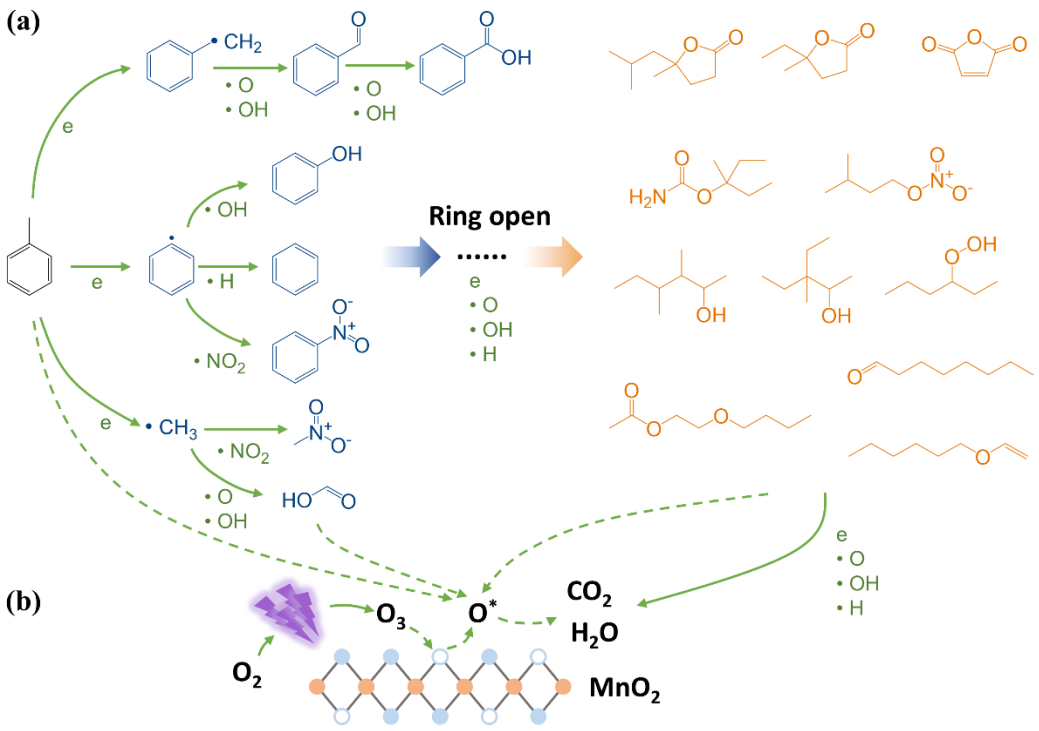

Fig. 11. Plausible reaction pathways for toluene decomposition in the PPC process: (a) NTP induced gas-phase reactions in the DBD reactor and (b) catalytic reactions on the surface of MnO_2 in the catalytic reactor.

The adsorption and oxidation of residual toluene and plasma-induced intermediates on the surface of hollow urchin α-MnO_2 is essential for the high mineralization rate of toluene. Ozone generated by electrical discharge can be converted into active oxygen species (O^*) over oxygen vacancies on the catalyst surface [48]. The remaining toluene and ring-opening byproducts can be adsorbed on the catalyst surface and react with the active oxygen from ozone conversion [49]. Hollow urchin α-MnO_2 with large surface area, high oxygen vacancy density and good low-temperature reducibility are favorable for the conversion of ozone conversion (~100%). Consequently, the integration of plasma with hollow urchin α-MnO_2 catalyst

significantly enhances the oxidation of toluene and reduces the formation of organic intermediates.

4. Conclusion

In this work, we develop a 3D hollow urchin α-MnO_2 for post-plasma catalytic decomposition of toluene. Hollow urchin nanoarchitecture is successfully constructed by well-defined 1D nanorods in a one-step hydrothermal route without any templates. The hollow structure can enlarge the contact surface area exposed to gas and extend gas retention time on the catalyst surface. The fully exposed non-agglomerated 1D α-MnO_2 nanorods can promote the oxygen vacancy density and low-temperature reducibility. The enhanced adsorption towards gas and the improved catalytic activity can facilitate the conversion of ozone into active oxygen species (~100%), promoting the oxidation of toluene and organic intermediates. As a result, hollow urchin α-MnO_2 exhibits higher toluene decomposition, CO_2 selectivity and carbon balance in comparison to solid urchin α-MnO_2. Specifically, coupling NTP with hollow urchin α-MnO_2 leads to excellent toluene decomposition of ~100%, CO_2 selectivity of ~59% and carbon balance of ~81% at an SIE of 240 J L^{-1}, which are 43%, 96% and 44% higher than that of NTP process, respectively. The energy efficiency is also enhanced by 64% compared with NTP process, reaching 13.1 g kWh^{-1} at an SIE of 119 J L^{-1}. Thus, the preeminent catalytic performance demonstrates that 3D hollow urchin nanostructure is a promising candidate for effective air purification in the plasma-catalytic system.

Acknowledgement

The authors acknowledge the financial support from the National Natural Science Foundation of China (No. 51722604) and the China Postdoctoral Science Foundation (No. 2019M662048). The authors would like to thank Tengfei Liu and Jucan Gao from the Center for Synthetic Biology at Zhejiang University for help with GC-MS.

Appendix A. Supplementary data

Supplementary material related to this article can be found in the online version.

References

[1] W. Chung, D. Mei, X. Tu, M. Chang, Removal of VOCs from gas streams via plasma and catalysis, Cat. Rev. 61 (2019) 270-331.

[2] H. L. Chen, H. M. Lee, S. H. Chen, M. B. Chang, S. J. Yu, S. N. Li, Removal of volatile organic compounds by single-stage and two-stage plasma catalysis systems: a review of the performance enhancement mechanisms, current status, and suitable applications, Environ. Sci. Technol. 43 (2009) 2216-2227.

[3] X. Feng, H. Liu, C. He, Z. Shen, T. Wang, Synergistic effects and mechanism of a non-thermal plasma catalysis system in volatile organic compound removal: a review, Catal. Sci. Technol. 8 (2017) 936-954.

[4] J. V. Durme, J. Dewulf, C. Leys, H. V. Langenhove, Combining non-thermal plasma with heterogeneous catalysis in waste gas treatment: A review, Appl. Catal., B 78 (2008) 324-333.

[5] A. M. Vandenbroucke, R. Morent, G. N. De, C. Leys, Non-thermal plasmas for non-catalytic and catalytic VOC abatement, J. Hazard. Mater. 195 (2011) 30.

[6] H. H. Kim, Y. Teramoto, N. Negishi, A. Ogata, A multidisciplinary approach to understand the interactions of nonthermal plasma and catalyst: A review, Catal. Today 256 (2015) 13-22.

[7] A. M. Harling, D. Glover, J. C. Whitehead, K. Zhang, The Role of ozone in the plasma-catalytic destruction of environmental pollutants, Appl. Catal., B 90 (2009) 157-161.

[8] J. V. Durme, J. Dewulf, W. Sysmans, C. Leys, H. V. Langenhove, Efficient toluene abatement in indoor air by a plasma catalytic hybrid system, Appl. Catal., B 74 (2007) 161-169.

[9] H. Huang, D. Ye, D. Y. C. Leung, F. Feng, X. Guan, Byproducts and pathways of toluene destruction via plasma-catalysis, J. Mol. Catal. A 336 (2011) 87-93.

[10] Z. Ye, J. M. Giraudon, N. D. Geyter, R. Morent, J. F. Lamonier, The design of MnO_x based catalyst in post-plasma catalysis configuration for toluene abatement, Catalysts 8 (2018) 91.

[11] Z. Bo, S. Yang, J. Kong, J. Zhu, Y. Wang, H. Yang, X. Li, J. Yan, K. Cen, X. Tu, Solar-enhanced

plasma-catalytic oxidation of toluene over a bifunctional graphene fin foam decorated with nanofin-like MnO_2, ACS Catal. 10 (2020) 4420-4432.

[12] M. T. Nguyen Dinh, J. M. Giraudon, A. M. Vandenbroucke, R. Morent, G. N. De, J. F. Lamonier, Manganese oxide octahedral molecular sieve K-OMS-2 as catalyst in post plasma-catalysis for trichloroethylene degradation in humid air, J. Hazard. Mater. 314 (2016) 88-94.

[13] C. Subrahmanyam, A. Renken, L. Kiwi-Minsker, Catalytic non-thermal plasma reactor for abatement of toluene, Chem. Eng. J. 160 (2010) 677-682.

[14] S. Sultana, A. Vandenbroucke, M. Mora, C. Jiménez-Sanchidrián, F. Romero-Salguero, C. Leys, N. De Geyter, R. Morent, Post plasma-catalysis for trichloroethylene decomposition over CeO_2 catalyst: Synergistic effect and stability test, Appl. Catal., B 253 (2019) 49-59.

[15] B. Dhandapani, S. T. Oyama, Gas phase ozone decomposition catalysts, Appl. Catal., B 11 (1997) 129-166.

[16] Y. Li, Z. Fan, J. Shi, Z. Liu, W. Shangguan, Post plasma-catalysis for VOCs degradation over different phase structure MnO_2 catalysts, Chem. Eng. J. 241 (2014) 251-258.

[17] J. Jarrige, P. Vervisch, Plasma-enhanced catalysis of propane and isopropyl alcohol at ambient temperature on a MnO_2-based catalyst, Appl. Catal., B 90 (2009) 74-82.

[18] S. Delagrange, L. Pinard, J. M. Tatibouët, Combination of a non-thermal plasma and a catalyst for toluene removal from air: Manganese based oxide catalysts, Appl. Catal., B 68 (2006) 92-98.

[19] Y. Huang, S. Dai, F. Feng, X. Zhang, Z. Liu, K. Yan, A comparison study of toluene removal by two-stage DBD-catalyst systems loading with MnO_x, $CeMnO_x$, and $CoMnO_x$, Environ. Sci. Pollut. Res. 22 (2015) 19240-19250.

[20] X. Yao, J. Zhang, X. Liang, C. Long, Plasma-catalytic removal of toluene over the supported manganese oxides in DBD reactor: Effect of the structure of zeolites support, Chemosphere 208 (2018) 922-930.

[21] C. C. Nguyen, N. N. Vu, T. O. Do, Recent advances in the development of sunlight-driven hollow structure photocatalysts and their applications, J. Mater. Chem. A 3 (2015) 18345-18359.

[22] P. Zhang, X. Lou, Design of heterostructured hollow photocatalysts for solar-to-chemical energy conversion, Adv. Mater. 31 (2019) 1900281.

[23] S. W. L. Ng, G. Yilmaz, L. O. Wei, G. W. Ho, One-step activation towards spontaneous etching of hollow and hierarchical porous carbon nanospheres for enhanced pollutant adsorption and energy storage, Appl. Catal., B 220 (2017).

[24] X. He, H. Sun, M. Zhu, M. Yaseen, D. Liao, X. Cui, H. Guan, Z. Tong, Z. Zhao, N-Doped porous graphitic carbon with multi-flaky shell hollow structure prepared using a green and 'useful'template of $CaCO_3$ for VOC fast adsorption and small peptide enrichment, Chem. Commun. 53 (2017) 3442-3445.

[25] X. Tan, Y. Wan, Y. Huang, C. He, Z. Zhang, Z. He, L. Hu, J. Zeng, D. Shu, Three-dimensional MnO_2 porous hollow microspheres for enhanced activity as ozonation catalysts in degradation of bisphenol A, J. Hazard. Mater. 321 (2017) 162-172.

[26] F. Wang, H. Dai, J. Deng, G. Bai, K. Ji, Y. Liu, Manganese oxides with rod-, wire-, tube-, and flower-like morphologies: highly effective catalysts for the removal of toluene, Environ. Sci. Technol. 46 (2012) 4034-4041.

[27] D. Li, Y. Zhu, H. Wang, Y. Ding, Nanoporous gold as an active low temperature catalyst toward CO oxidation in hydrogen-rich stream, Sci. Rep. 3 (2013) 1-7.

[28] B. Li, G. Rong, Y. Xie, L. Huang, C. Feng, Low-temperature synthesis of α-MnO_2 hollow urchins and their application in rechargeable Li^+ batteries, Inorg. Chem. 45 (2006) 6404-6410.

[29] M. Xu, L. Kong, W. Zhou, H. Li, Hydrothermal synthesis and pseudocapacitance properties of α-MnO_2 hollow spheres and hollow urchins, J. Phys. Chem. C 111 (2007) 19141-19147.

[30] W. Xiao, D. Wang, X. W. Lou, Shape-controlled synthesis of MnO_2 nanostructures with enhanced electrocatalytic activity for oxygen reduction, J. Phys. Chem. C 114 (2010) 1694-1700.

[31] M. Zhou, X. Zhang, J. Wei, S. Zhao, L. Wang, B. Feng, Morphology-controlled synthesis and novel microwave absorption properties of hollow urchinlike α-MnO_2 nanostructures, J. Phys. Chem. C 115 (2011) 1398-1402.

[32] L. Gang, Y. Lu, L. Cheng, M. Zhu, C. Zhai, Y. Du, Y. Ping, Efficient catalytic ozonation of bisphenol-A over reduced graphene oxide modified sea urchin-like α-MnO_2 architectures, J. Hazard. Mater. 294 (2015) 201-208.

[33] S. Zhao, T. Liu, D. Shi, Y. Zhang, W. Zeng, T. Li, B. Miao, Hydrothermal synthesis of urchin-like MnO_2 nanostructures and its electrochemical character for supercapacitor, Appl. Surf. Sci. 351 (2015) 862-868.

[34] P. Ragupathy, D. H. Park, G. Campet, H. Vasan, S. J. Hwang, J. H. Choy, N. Munichandraiah, Remarkable capacity retention of nanostructured manganese oxide upon cycling as an electrode material for supercapacitor, J. Phys. Chem. C 113 (2009) 6303-6309.

[35] J. Luo, H. Zhu, H. Fan, J. Liang, H. Shi, G. Rao, J. Li, Z. Du, Z. Shen, Synthesis of single-crystal tetragonal α-MnO_2 nanotubes, J. Phys. Chem. C 112 (2008) 12594-12598.

[36] C. Yu, G. Li, L. Wei, Q. Fan, Q. Shu, C. Y. Jimmy, Fabrication, characterization of β-MnO_2 microrod catalysts and their performance in rapid degradation of dyes of high concentration, Catal. Today 224 (2014) 154-162.

[37] G. Zhu, J. Zhu, W. Jiang, Z. Zhang, J. Wang, Y. Zhu, Q. Zhang, Surface oxygen vacancy induced α-MnO_2 nanofiber for highly efficient ozone elimination, Appl. Catal., B 209 (2017) 729-737.

[38] A. Kumar, A. Sanger, A. Kumar, Y. Kumar, R. Chandra, An efficient α-MnO_2 nanorods forests electrode for electrochemical capacitors with neutral aqueous electrolytes, Electrochim. Acta 220 (2016) 712-720.

[39] J. Hou, Y. Li, L. Liu, L. Ren, X. Zhao, Effect of giant oxygen vacancy defects on the catalytic oxidation of OMS-2 nanorods, J. Mater. Chem. A 1 (2013) 6736-6741.

[40] S. J. Shih, R. Sharghi-Moshtaghin, M. R. De Guire, R. Goettler, Z. Xing, Z. Liu, A. H. Heuer, Mn valence determination for lanthanum strontium manganite solid oxide fuel cell cathodes, J. Electrochem. Soc. 158 (2011) B1276-B1280.

[41] Y. Yang, J. Huang, S. Wang, S. Deng, B. Wang, G. Yu, Catalytic removal of gaseous unintentional POPs on manganese oxide octahedral molecular sieves, Appl. Catal., B 142 (2013) 568-578.

[42] S. Rong, P. Zhang, Y. Yang, L. Zhu, J. Wang, F. Liu, MnO_2 framework for instantaneous mineralization of carcinogenic airborne formaldehyde at room temperature, ACS Catal. 7 (2017) 1057-1067.

[43] E. Rezaei, J. Soltan, Low temperature oxidation of toluene by ozone over MnO_x/γ-alumina and MnO_x/MCM-41 catalysts, Chem. Eng. J. 198–199 (2012) 482-490.

[44] E. Rezaei, J. Soltan, N. Chen, Catalytic oxidation of toluene by ozone over alumina supported manganese oxides: Effect of catalyst loading, Appl. Catal., B 136-137 (2013) 239-247.

[45] L. Lu, H. Tian, J. He, Q. Yang, Graphene–MnO_2 hybrid nanostructure as a new catalyst for formaldehyde oxidation, J. Phys. Chem. C 120 (2016) 23660-23668.

[46] Y. Li, Z. Fan, J. Shi, Z. Liu, J. Zhou, W. Shangguan, Modified manganese oxide octahedral molecular sieves M′-OMS-2 (M′=Co,Ce,Cu) as catalysts in post plasma-catalysis for acetaldehyde degradation, Catal. Today 256 (2015) 178-185.

[47] J. Ma, C. Wang, H. He, Transition metal doped cryptomelane-type manganese oxide catalysts for ozone decomposition, Appl. Catal., B 201 (2017) 503-510.

[48] J. Jia, P. Zhang, L. Chen, Catalytic decomposition of gaseous ozone over manganese dioxides with different crystal structures, Appl. Catal., B 189 (2016) 210-218.

[49] J. Li, H. Na, X. Zeng, T. Zhu, Z. Liu, In situ DRIFTS investigation for the oxidation of toluene by ozone over Mn/HZSM-5, Ag/HZSM-5 and Mn–Ag/HZSM-5 catalysts, Appl. Surf. Sci. 311 (2014) 690-696.

[50] Y. Yang, J. Jia, Y. Liu, P. Zhang, The effect of tungsten doping on the catalytic activity of α-MnO_2 nanomaterial for ozone decomposition under humid condition, Appl. Catal., A 562 (2018) 132-141.

[51] G. Zhu, J. Zhu, W. Li, W. Yao, R. Zong, Y. Zhu, Q. Zhang, Tuning the K^+ concentration in the tunnels of α-MnO_2 to increase the content of oxygen vacancy for ozone elimination, Environ. Sci. Technol. 52 (2018) 8684-8692.

[52] C. K. Sang, G. S. Wang, Catalytic combustion of VOCs over a series of manganese oxide catalysts, Appl. Catal., B 98 (2010) 180-185.

[53] W. Si, Y. Wang, Y. Peng, X. Li, K. Li, J. Li, A high-efficiency γ-MnO_2-like catalyst in toluene combustion, Chem. Commun. 51 (2015) 14977-14980.

[54] A. Vinu, D. P. Sawant, K. Ariga, M. Hartmann, S. Halligudi, Benzylation of benzene and other aromatics by benzyl chloride over mesoporous AlSBA-15 catalysts, Microporous Mesoporous Mater. 80 (2005) 195-203.

[55] X. Yao, Y. Li, Z. Fan, Z. Zhang, M. Chen, W. Shangguan, Plasma catalytic removal of hexanal over Co–Mn solid solution: effect of preparation method and synergistic reaction of ozone, Ind. Eng. Chem. Res. 57 (2018) 4214-4224.

[56] J. J. Chen, C. Sun, Z. Huang, F. Qjn, H. L. Xu, W. Shen, Fabrication of functionalized porous silica nanocapsules with a hollow structure for high performance of toluene adsorption-desorption, ACS Omega 5 (2020) 5805-5814.

[57] K. Kosuge, S. Kubo, N. Kikukawa, M. Takemori, Effect of pore structure in mesoporous silicas on VOC dynamic adsorption/desorption performance, Langmuir 23 (2007) 3095-3102.

[58] S. Sultana, Z. Ye, S. K. Veerapandian, A. Löfberg, N. De Geyter, R. Morent, J.-M. Giraudon, J.-F. Lamonier, Synthesis and catalytic performances of K-OMS-2, Fe/K-OMS-2 and Fe-K-OMS-2 in post plasma-catalysis for dilute TCE abatement, Catal. Today 307 (2018) 20-28.

[59] X. Lin, S. Li, H. He, Z. Wu, J. Wu, L. Chen, D. Ye, M. Fu, Evolution of oxygen vacancies in MnO_x-CeO_2 mixed oxides for soot oxidation, Appl. Catal., B 223 (2018) 91-102.

[60] X. Fan, T. L. Zhu, M. Y. Wang, X. M. Li, Removal of low-concentration BTX in air using a combined plasma catalysis system, Chemosphere 75 (2009) 1301-1306.

[61] H. Q. Trinh, Y. S. Mok, Plasma-catalytic oxidation of acetone in annular porous monolithic ceramic-supported catalysts, Chem. Eng. J. 251 (2014) 199-206.

[62] N. Jiang, Y. Zhao, C. Qiu, K. Shang, N. Lu, J. Li, Y. Wu, Y. Zhang, Enhanced catalytic performance of CoO_x-CeO_2 for synergetic degradation of toluene in multistage sliding plasma

system through response surface methodology (RSM), Appl. Catal., B 259 (2019) 118061.

[63] T. Chang, Z. Shen, Y. Huang, J. Lu, D. Ren, J. Sun, J. Cao, H. Liu, Post-plasma-catalytic removal of toluene using MnO_2-Co_3O_4 catalysts and their synergistic mechanism, Chem. Eng. J. 34 (2018) 15-25.

[64] H. Huang, D. Ye, Combination of photocatalysis downstream the non-thermal plasma reactor for oxidation of gas-phase toluene, J. Hazard. Mater. 171 (2009) 535-541.

[65] X. Fan, T. Zhu, Y. Wan, X. Yan, Effects of humidity on the plasma-catalytic removal of low-concentration BTX in air, J. Hazard. Mater. 180 (2010) 616-621.

[66] M. Magureanu, D. Piroi, N. B. Mandache, V. I. Pârvulescu, V. Pârvulescu, B. Cojocaru, C. Cadigan, R. Richards, H. Daly, C. Hardacre, In situ study of ozone and hybrid plasma Ag–Al catalysts for the oxidation of toluene: Evidence of the nature of the active sites, Appl. Catal., B 104 (2011) 84-90.

[67] H. Huang, D. Ye, X. Guan, The simultaneous catalytic removal of VOCs and O_3 in a post-plasma, Catal. Today 139 (2008) 43-48.

[68] A. M. Harling, V. Demidyuk, S. J. Fischer, J. C. Whitehead, Plasma-catalysis destruction of aromatics for environmental clean-up: Effect of temperature and configuration, Appl. Catal., B 82 (2008) 180-189.

[69] A. M. Vandenbroucke, M. N. Dinh, N. Nuns, J. M. Giraudon, N. De Geyter, C. Leys, J. F. Lamonier, R. Morent, Combination of non-thermal plasma and Pd/$LaMnO_3$ for dilute trichloroethylene abatement, Chem. Eng. J. 283 (2016) 668-675.

[70] H. Zhang, F. Zhu, X. Li, R. Xu, L. Li, J. Yan, X. Tu, Steam reforming of toluene and naphthalene as tar surrogate in a gliding arc discharge reactor, J. Hazard. Mater. 369 (2019) 244-253.

[71] W. Chen, J. Huang, N. Du, X. Liu, X. Wang, G. Lv, G. Zhang, L. Guo, S. Yang, Treatment of enterococcus faecalis bacteria by a helium atmospheric cold plasma brush with oxygen addition, J. Appl. Phys. 112 (2012) 013304.

[72] X. Xu, P. Wang, W. Xu, J. Wu, L. Chen, M. Fu, D. Ye, Plasma-catalysis of metal loaded SBA-15 for toluene removal: comparison of continuously introduced and adsorption-discharge plasma system, Chem. Eng. J. 283 (2016) 276-284.

[73] X. Zhu, S. Zhang, Y. Yang, C. Zheng, J. Zhou, X. Gao, X. Tu, Enhanced performance for plasma-catalytic oxidation of ethyl acetate over $La_{1-x}Ce_xCoO_{3+\delta}$ catalysts, Appl. Catal., B 213 (2017) 97-105.

[74] N. Jiang, J. Hu, J. Li, K. Shang, N. Lu, Y. Wu, Plasma-catalytic degradation of benzene over Ag–Ce bimetallic oxide catalysts using hybrid surface/packed-bed discharge plasmas, Appl. Catal., B 184 (2016) 355-363.

[75] L. Ye, F. Feng, J. Liu, X. Tang, X. Zhang, Y. Huang, Z. Liu, K. Yan, Toluene decomposition by a two-stage hybrid plasma catalyst system in dry air, IEEE Trans. Plasma Sci. 42 (2014) 3529-3538.

[76] M. D. Hernández-Alonso, I. Tejedor-Tejedor, J. M. Coronado, M. A. Anderson, Operando FTIR study of the photocatalytic oxidation of methylcyclohexane and toluene in air over TiO_2–ZrO_2 thin films: Influence of the aromaticity of the target molecule on deactivation, Appl. Catal., B 101 (2011) 283-293.

[77] W. Xu, N. Wang, Y. Chen, J. Chen, X. Xu, L. Yu, L. Chen, J. Wu, M. Fu, A. Zhu, In situ FT-IR study and evaluation of toluene abatement in different plasma catalytic systems over metal oxides loaded γ-Al_2O_3, Catal. Commun. 84 (2016) 61-66.

[78] H. Yi, X. Yang, X. Tang, S. Zhao, X. Xie, T. Feng, Y. Ma, X. Cui, Performance and pathways of toluene degradation over Co/13X by different processes based on nonthermal plasma, Energy Fuels 31 (2017) 11217-11224.

[79] A. Rodrigues, J. M. Tatibouët, E. Fourré, Operando DRIFT spectroscopy characterization of intermediate species on catalysts surface in VOC removal from air by non-thermal plasma assisted catalysis, Plasma Chem. Plasma Process. 36 (2016) 901-915.

[80] X. Yao, N. Jiang, J. Li, N. Lu, K. Shang, Y. Wu, An improved corona discharge ignited by oxide cathodes with high secondary electron emission for toluene degradation, Chem. Eng. J. 362 (2019) 339-348.

[81] A. Ogata, D. Ito, K. Mizuno, S. Kushiyama, A. Gal, T. Yamamoto, Effect of coexisting components on aromatic decomposition in a packed-bed plasma reactor, Appl. Catal., A 236 (2002) 9-15.